Magnetotail origins of auroral Alfvénic power

B. Zhang,[1] W. Lotko,[1] O. Brambles,[1] P. Damiano,[1,2] M. Wiltberger,[3] and J. Lyon[4]

Received 6 March 2012; revised 2 July 2012; accepted 24 July 2012; published 6 September 2012.

[1] The generation of Alfvénic Poynting flux in the central plasma sheet and its polar distribution at low altitude are studied using three dimensional global simulations of the solar wind-magnetosphere-ionosphere interaction. A 24-hour event simulation (4–5 Feb 2004) driven by solar wind and interplanetary magnetic field data reproduces the global morphology of Alfvénic Poynting flux measured by the Polar satellite, including its dawn-dusk asymmetry. Controlled simulations show that the dawn-dusk asymmetry is regulated by the spatial variation in ionospheric conductance. The asymmetry disappears when the conductance is taken to be spatially uniform. The simulated Alfvénic Poynting flux is generated in the magnetotail by time-variable, fast flows emerging from nightside reconnection. The simulated fast flows are more intense in the premidnight sector as observed; this asymmetry also disappears when the ionospheric conductance is spatially uniform. Analysis of the wave propagation in the plasma sheet source region, near $x_{GSM} \approx -15$ R_E, shows that as the fast flow brakes, a portion of its kinetic energy is transformed into the electromagnetic energy of intermediate and fast magnetohydrodynamic waves. The wave power is dominantly compressional in the source region and becomes increasingly Alfvénic as it propagates along magnetic field lines toward the ionosphere.

Citation: Zhang, B., W. Lotko, O. Brambles, P. Damiano, M. Wiltberger, and J. Lyon (2012), Magnetotail origins of auroral Alfvénic power, *J. Geophys. Res.*, *117*, A09205, doi:10.1029/2012JA017680.

1. Introduction

[2] Nondispersive Alfvén waves can propagate with low loss across the vast reaches of geospace. Of particular interest is their capacity to transmit electromagnetic power generated by solar wind and magnetospheric dynamos to low-altitude absorption layers where the wave energy is converted to particle beams and heat. Alfvén waves are magnetically guided to a high degree so their low-altitude amplitude distributions reflect the spatial structure of their generators.

[3] The global morphology of Alfvén wave power flowing to low altitudes has been derived from electric and magnetic fields measured on the polar orbiting FAST [*Chaston et al.*, 2003] and Polar [*Keiling et al.*, 2003] satellites. The FAST satellite sampled Alfvénic Poynting fluxes at altitudes of 2000 to 4200 km where much of the Alfvén wave energy is converted to accelerated particles. With apogee at 9 R_E, the Polar satellite was able to sample the amplitude distribution of Alfvénic Poynting fluxes above the absorption layers traversed by FAST.

[4] In deriving the Alfvénic Poynting flux from data acquired on an orbiting platform, the electric and magnetic fields must be filtered in a frequency band that captures the intrinsic time variation of the waves as well as satellite Doppler shifted spatial structure of longer period Alfvén waves. The data reduction should also minimize standing wave components resulting from wave reflection at the ionosphere. The bandpass filter appropriate for the altitude of the Polar measurements resolves waves with periods in the range 6–180 s [*Keiling et al.*, 2000; *Wygant et al.*, 2000]. In this passband, Alfvén wave activity is observed with the highest intensities in the nightside auroral zone and dayside cusp region. A one-year average of the Alfvénic Poynting flux recorded by the Polar satellite exhibits higher intensity fluxes in the premidnight auroral zone relative to the postmidnight region [*Keiling et al.*, 2003]. This significant dawn-dusk asymmetry in Alfvénic Poynting flux is evidently a robust feature of the magnetosphere-ionosphere (MI) system. It appears in statistical patterns derived from 4 years of FAST measurements of both Alfvén wave energy flux and associated field-aligned electron energy flux [*Chaston et al.*, 2003] and in ten-year averages of precipitating "broadband" electron energy flux derived from DMSP satellite measurements [*Newell et al.*, 2009]. The dawn-dusk asymmetry in wave power flowing into the low-altitude auroral region presumably reflects asymmetries in the plasma sheet dynamo processes generating the Alfvén wave power, but the causes of this asymmetry have not been studied and remain unknown.

[1]Thayer School of Engineering, Dartmouth College, Hanover, New Hampshire, USA.
[2]Now at Princeton Plasma Physics Lab, Princeton, New Jersey, USA.
[3]High Altitude Observatory, National Center for Atmospheric Research, Boulder, Colorado, USA.
[4]Department of Physics and Astronomy, Dartmouth College, Hanover, New Hampshire, USA.

Corresponding author: B. Zhang, Thayer School of Engineering, Dartmouth College, 14 Engineering Dr., Hanover, NH 03755, USA. (bzhang@dartmouth.edu)

©2012. American Geophysical Union. All Rights Reserved.
0148-0227/12/2012JA017680

[5] *Angelopoulos et al.* [2002] investigated the generation of auroral Alfvén wave pulses in the plasma sheet during a substorm event. The pulses were recorded contemporaneously by the Polar satellite at altitudes of $\sim$5 R_E and the Geotail satellite at altitudes of $\sim$18 R_E in the central plasma sheet. They identify earthward-directed, bursty bulk flows (BBFs) in the plasma sheet as the primary energy source for the Alfvén waves in this event [*Angelopoulos et al.*, 1992]. BBFs are fast convective flows (several hundreds of kilometers per second) typically of 10 min duration or longer with individual peaks of the order of 1 minute [*Angelopoulos et al.*, 1992]. In the *Angelopoulos et al.* [2002] study, the electromagnetic energy carried by the Alfvén waves was found to be a small portion of the kinetic energy in the BBFs. The wave power measured in the Alfvén wave frequency band at the lower altitude of Polar was also an order of magnitude smaller than the magnetically mapped power measured in the same band at Geotail. This finding, combined with an estimate for the wave impedance at Geotail that exceeded the local Alfvén speed, led Angelopoulos to conclude: i) the observed waves are kinetic Alfvén waves, and ii) the waves encounter substantial electron Landau damping in their transit between the Geotail and Polar satellites. If Landau damping is responsible for the wave attenuation between satellites, one would expect to see accelerated electrons on the same field lines as the Alfvén wave Poynting fluxes. That fast streams of field-aligned electrons did not accompany the reduction in Alfvénic power between Geotail and Polar was attributed to the low temporal resolution of the electron measurements on Polar and to temporal aliasing of the electron measurements on Geotail.

[6] Earthward flow bursts in the magnetotail are also closely associated with auroral brightenings in the high-latitude upper atmosphere [*Fairfield et al.*, 1999; *Zesta et al.*, 2000]. The morphology of auroral brightenings called poleward boundary intensifications [*Nishimura et al.*, 2010] is similar to that of Alfvénic power flowing into the nightside ionosphere. The electron precipitation that causes auroral brightenings typically carries upward field-aligned currents, and it is well known that changes in field-aligned current are communicated by Alfvén waves [e.g., *Lysak*, 1990]. Although auroral intensifications and magnetotail flow bursts are most intense during substorm events [*Baumjohann et al.*, 1990; *Angelopoulos et al.*, 1992], they also occur during quiet times and during intervals of steady magnetospheric convection [*Sergeev et al.*, 1996]. The most plausible cause of plasma sheet flow bursts is spatially and temporally variable nightside reconnection [*Sergeev et al.*, 1992; *Angelopoulos et al.*, 1996; *Nagai et al.*, 1998]. Flow bursts are deflected and decelerated by the strong outward pressure force near the inner edge of the plasma sheet [*Shiokawa et al.*, 1997]. The braking is accompanied by oscillatory compressions in the flow and Alfvén wave activity known as Pi 2 pulsations [*Shiokawa et al.*, 1998; *Kepko et al.*, 2001]. As the flow burst brakes, its kinetic energy is transformed into electromagnetic energy through the generation of fast magnetohydrodynamic waves and shear Alfvén waves that carry field-aligned currents to the ionosphere [*Volwerk et al.*, 2007].

[7] The distribution of BBF events in the plasma sheet cluster in the 2100–0100 MLT sector with a centroid near 2300 MLT [*McPherron et al.*, 2011]. Given the statistical distribution of BBFs, the event study by *Angelopoulos et al.* [2002] connecting an Alfvén wave burst at Polar satellite altitudes with BBFs in the plasma sheet and the propensity of braking BBFs to generate Alfvén wave and associated auroral activity, it seems plausible that the dawn-dusk asymmetry in the distribution of Alfvén wave power reported by *Keiling et al.* [2003] is connected with the dawn-dusk asymmetry in the plasma sheet distribution of BBFs. But why are both most prevalent in the premidnight sector?

[8] We know that the nightside distribution of ionospheric conductivity exhibits significant meridional gradients [*Hardy et al.*, 1987; *Fuller-Rowell and Evans*, 1987] which cause the polar ionospheric convection pattern to rotate clockwise [*Yasuhara et al.*, 1983]. We propose the hypothesis here that the distribution of ionospheric conductance and its effect on high-latitude convection regulates the distributions of plasma sheet flow bursts and auroral Alfvénic power. It is difficult to test this hypothesis with the sparse measurements available in geospace. In order to conduct such a study, one would need events with essentially the same solar wind and IMF driving conditions for different ionospheric states, especially different ionospheric conductances. Satellites recording Alfvén wave activity and BBFs would have to be approximately on the same magnetic field line connecting the plasma sheet region and the ionosphere for these special conditions. These requirements make it very difficult observationally to determine the effects of the ionosphere on magnetotail dynamics. Consequently, we will use simulations to test the proposed hypothesis.

[9] Global models of the solar wind-magnetosphere-ionosphere interaction can be used to follow the temporal evolution of fields and plasmas in the magnetosphere driven by solar wind conditions derived from actual upstream satellite data. Controlled numerical experiments can be designed to isolate the effects of magnetosphere-ionosphere coupling on the system dynamics, including the type of asymmetries described above. In this paper, we use the three-dimensional Lyon-Fedder-Mobarry (LFM) global simulation model [*Lyon et al.*, 2004] to examine the generation of Alfvénic power in the central plasma sheet and to test the hypothesis that the ionosphere regulates the dawn-dusk asymmetry observed in auroral Alfvénic power.

[10] Two types of simulation studies are conducted. The first is a 24-hour event simulation with upstream conditions derived from the NASA OMNI dataset. This simulation exhibits geomagnetic activity with average levels (as measured by the *Kp* index) similar to those in the statistical study of *Keiling et al.* [2003]. The results provide a statistical sample of simulated Alfvén wave activity that can be compared directly with the Polar satellite statistical distributions. The second simulation study involves controlled experiments that eliminate all asymmetries and variability in solar wind driving so as to isolate the effects of different ionospheric states on the simulated distributions of auroral Alfvén wave activity and their magnetotail generators.

[11] The next sections of the paper are organized as follows: 2. Compare global distributions of observed and simulated Alfvénic Poynting flux. 3. Evaluate effects of ionospheric conductance using controlled simulations. 4. Examine the generation of Alfvénic Poynting flux in the magnetotail. 5. Analyze propagation of Alfvénic power from

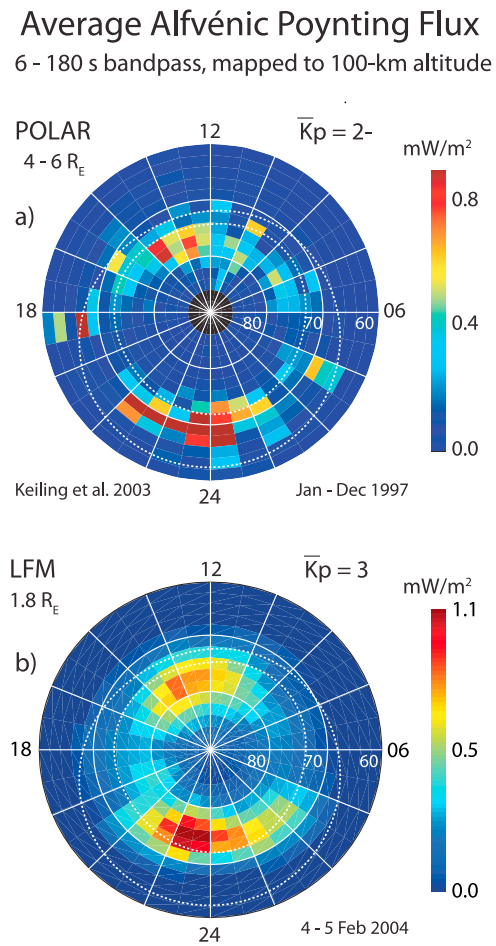

Figure 1. Global morphology of downward Alfvénic Poynting flux from (a) a one-year average derived from Polar spacecraft measurements [*Keiling et al.*, 2003], and (b) a 24-hour average derived from the LFM global simulation running from 1200 UT, 04-Feb-2004 to 1200 UT, 05-Feb-2004. The white curves in both figures show the *Feldstein and Starkov* [1967] statistical auroral oval.

the plasma sheet to low altitude. 6. Summarize results and conclusions.

2. Morphology of Alfvénic Poynting Fluxes

[12] The global morphology of Alfvénic Poynting flux was analyzed by *Keiling et al.* [2003] for the complete set of 470 Polar satellite orbits in 1997 when the satellite's high inclination over the northern polar cap was between 25,000 km and 38,000 km above the ground. The field-aligned Poynting flux was calculated from measured, perturbation electric ($\delta\mathbf{E}$) and magnetic ($\delta\mathbf{B}$) fields as

$$S_{\|} = \frac{1}{\mu_0}\delta\mathbf{E} \times \delta\mathbf{B} \cdot \frac{\mathbf{B}}{\mathrm{B}} \tag{1}$$

where μ_0 is the permeability of free space, and $\mathbf{B}$ is the mean vector magnetic field calculated from a 180-s running average of the locally measured magnetic field. Perturbation $\delta\mathbf{E}$ and $\delta\mathbf{B}$ were calculated by subtracting a 180-s running average of each measured field from 6-s averages of each field. To reduce the effect of standing waves (e.g., superposition of incident and reflected waves resulting from interaction with the ionosphere), $S_{\|}$ was averaged over 30-s intervals. The resulting Poynting flux values were then projected to a reference ionospheric altitude of 100 km by mapping $S_{\|}/B$ = constant along IGRF model field lines. The full database of mapped $S_{\|}$ values was then separated into upgoing and downgoing fluxes with each sorted into 2° MLAT × 0.75 MLT (magnetic latitude × magnetic local time) bins.

[13] The average distribution of downgoing $S_{\|}$ reported by *Keiling et al.* [2003] is reproduced in Figure 1a. The results show that Alfvén-wave electromagnetic power statistically flows into the dayside cusp region and nightside auroral zone with a significant dawn-dusk asymmetry. The average Poynting fluxes exhibit two main regions of enhanced intensity. The dayside enhancement occurs between 1300–1500 MLT and 74°–80° MLAT. The nightside enhancement occurs in the premidnight auroral region between 2100–0100 MLT and 66°–76° MLAT.

[14] The average *Kp* index for all of 1997 was 2−. However, the average *Kp* for the intervals when the high-latitude data represented in Figure 1a were acquired may be different from the annual average. It is impractical to do a one year simulation of the global magnetosphere and compare its results to observations. Instead we can choose a sample event that has some statistical similarity with the year 1997. To compare Alfvénic Poynting fluxes derived from LFM simulations with the Polar results, a 24-hour simulation was performed for interplanetary plasma and magnetic field conditions given in the NASA OMNI 1-minute combined dataset for the interval 4 Feb 2004, 1200 UT to 5 Feb 2004, 1200 UT. The interval was selected for its moderate activity level with *Kp* ranging from 3− to 3+ and a mean of 3. Although the average *Kp* index for year 1997 was 2−, active time periods with higher *Kp* value definitely contributed to the observations. Therefore, the *Kp* 3 event was selected instead of a *Kp* 2− event. A description of the simulation method, grid and boundary conditions is included in Appendix A.

[15] The simulated Alfvénic Poynting flux was calculated from (1) using the electric and magnetic fields at grid cells near the inner boundary of the LFM simulation (at approximately 2.8 R_E geocentric and 0.8 R_E above the spherical low-altitude simulation boundary). This fiducial surface is chosen because the low-altitude boundary conditions in the simulation cause diversion of field-aligned into perpendicular Poynting flux near the low-altitude simulation boundary, whereas at $r \geq 2.8$ R_E the simulated AC Poynting fluxes are more nearly conserved with $S_{\|}/B \approx$ constant along field lines. The procedure for evaluating the mapped $S_{\|}$ in the simulation is the same as in the Polar study with minor exceptions: 1) Rather than computing 6-s average fields as in the Polar study, the values of simulated $\mathbf{E}$ and $\mathbf{B}$ are written to a data file every 5 s. These drop file values are used to calculate the perturbation and 180-s, running-average mean fields (comparatively little power resides at short periods in the simulations and Polar data so the choice of 5 s or 6 s sampling is relatively inconsequential); 2) $S_{\|}$ is averaged over one-minute intervals rather than 30-s intervals to remove standing waves. (The choice of either one-minute or 30-s averaging interval does not affect the average distribution of $S_{\|}$ in the

LFM simulation.) A simulation dataset of 24(hour) × 60 (minute) one-minute average samples of $S_{\|}$ is accumulated at each grid cell on the $r = 2.8$ R_E fiducial surface; 3) the 24 × 60 samples at each cell are then averaged to give a 24-hour average $S_{\|}$ at each grid cell on the $r = 2.8$ R_E fiducial surface; 4) the resulting average downward $S_{\|}$ is mapped to 100-km altitude along dipole rather than IGRF field lines taking $S_{\|}/B$ = constant as in the Polar study. The average magnetic field at altitudes below 2.8 R_E geocentric is dipolar in the simulation to a good approximation; and 5) the mapped, average values are then interpolated into 2° MLAT × 0.75 MLT ionospheric bins to produce a polar plot like the one in Figure 1a. The mapped simulation grid is actually about 50% denser than the 2° MLAT × 0.75 MLT ionospheric bins.

[16] The resulting distribution of average downward Alfvénic Poynting flux from the 24-hour simulation is shown in Figure 1b. The LFM simulation captures the prominent postnoon and premidnight enhancements evident in the morphology of the Polar study with comparable intensities in both studies. That the intensities are similar is somewhat surprising because the Polar measurements resolve intense dispersive Alfvén waves that are subgrid in the simulations. Furthermore, the physics of dispersive Alfvén waves is not included in the one-fluid MHD model of the simulations. Noteworthy differences in the Polar and simulation results include:

[17] 1. The simulated $S_{\|}$ on average is more intense than the Polar average values. This difference may be due to the higher average geomagnetic activity during the 24-hour LFM run (mean Kp = 3) relative to that of the one-year interval of the Polar study (mean Kp = 2−). The simulated intensities might be even higher if the simulations were able to resolve dispersive Alfvén waves.

[18] 2. The Polar results are more symmetric within ±0.75° MLT of midnight than the simulation results. We have found that simulated substorms generate more symmetric distributions of Alfvénic Poynting fluxes near midnight, while steady magnetospheric convection states (SMCs) exhibit the average asymmetry shown in Figure 1b (to be discussed in more detail below). The difference between Polar and simulation results near midnight would be expected if the data used in the one-year Polar study contains a higher percentage of substorms than the 24-hour simulation study.

[19] 3. The premidnight enhancement in Polar average fluxes occurs at lower latitude than that of LFM average fluxes. They peak near 69° MLAT and mainly lie within the Feldstein statistical auroral oval (white dotted curves) while the premidnight LFM fluxes peak near 75° MLAT with most of the distribution lying poleward of the Feldstein oval. This large offset may be due 1) to less stretching of the nightside plasma sheet in the LFM event simulation relative to the actual magnetosphere or 2) to inaccuracies in the IGRF mapping used by *Keiling et al.* [2003] to map the Polar fluxes from relatively high altitude where the field may deviate significantly from the IGRF, especially during the active periods producing the most intense Alfvén-wave fluxes. Two other observational studies differ in detail with the morphology reported by *Keiling et al.* [2003]. The statistical distribution of median peak values of dispersive Alfvén-wave Poynting fluxes derived from low-altitude FAST measurements peaks near 73° MLAT [*Chaston et al.*, 2003]. The statistical distribution of the energy flux of "broadband" electron precipitation in the 10-year DMSP particle data set exhibits a broad premidnight peak from 71°–77° MLAT for "high solar wind driving conditions" and a narrower and less intense peak near 72° MLAT for "low solar wind driving" [*Newell et al.*, 2009]. Broadband electron precipitation is attributed to electron acceleration by dispersive Alfvén waves and its MLT-MLAT distribution may be considered as a proxy for Alfvén wave energy flux [*Chaston et al.*, 2003]. These other results appear to be consistent with the higher latitude distribution of the intense Alfvénic Poynting fluxes in the simulation. Thus it is not clear at this juncture whether the Polar or LFM-simulated distributions are statistically more representative of the phenomena.

[20] 4. The Polar distribution exhibits flankside spots of Alfvénic activity at 1800–1845 MLT and 0345–0430 MLT that are absent in the simulated distribution. These enhancements in the Polar average fluxes may be a feature of the moderate storms that occurred in 1997 sample used by *Keiling et al.* [2003]. We have found in simulations that as the IMF B_z becomes more negative, nightside Alfvénic activity tends to spread toward the dawn and dusk meridians. The 24-hour simulated interval represented in Figure 1b contained no storms.

[21] However one views these differences, the degree of similarity in the observed and simulated distribution is actually remarkable and suggests that LFM simulations can be used to understand the origins of the observed Poynting fluxes. To this end, controlled numerical experiments were conducted to isolate cause and effect of features in the simulations that resemble the observations.

3. Cause of Dawn-Dusk Asymmetry

[22] A controlled 5-hour simulation was performed for steady interplanetary conditions with $B_x = B_y = 0$, $B_z = -5$ nT, $n = 5/\text{cm}^3$, $T = 10$ eV, $v_x = -400$ km/s and $v_y = v_z = 0$ at the upstream boundary of the LFM simulation domain at x_{GSE} = 30 R_E. No substorm events are observed during the last three hours of the simulation, and the magnetospheric convection becomes quasi-steady but still variable, as seen in animations of the time history of the convection and vorticity in the plasma sheet. It resembles the steady magnetospheric convection event simulated by *Pulkkinen et al.* [2010] using the LFM model, with characteristics similar to those shown in *Pulkkinen et al.* [2010, Figures 2 and 3].

[23] Before discussing the average properties of the Alfvénic Poynting fluxes in the idealized simulation, we note that the simulation exhibits considerable time variability, despite the imposed steady solar wind and IMF conditions [*Claudepierre et al.*, 2008]. Most of the variability occurs in the magnetotail and along the magnetopause boundary. The magnetopause boundary variations are most likely due to Kelvin-Helmholtz waves which develop large vortical structures along the magnetotail flanks. As these vortices evolve and expand, they interact with and modulate nightside reconnection, which causes, among other effects, variability in sunward-directed reconnection flows resembling bursty bulk flows [*Angelopoulos et al.*, 1992]. As discussed in the next section, this nightside variability generates bursty Alfvénic fluctuations which propagate along field lines to low altitudes. Figure 2 shows four snapshots in time of downward flowing Poynting fluxes calculated from (1) and

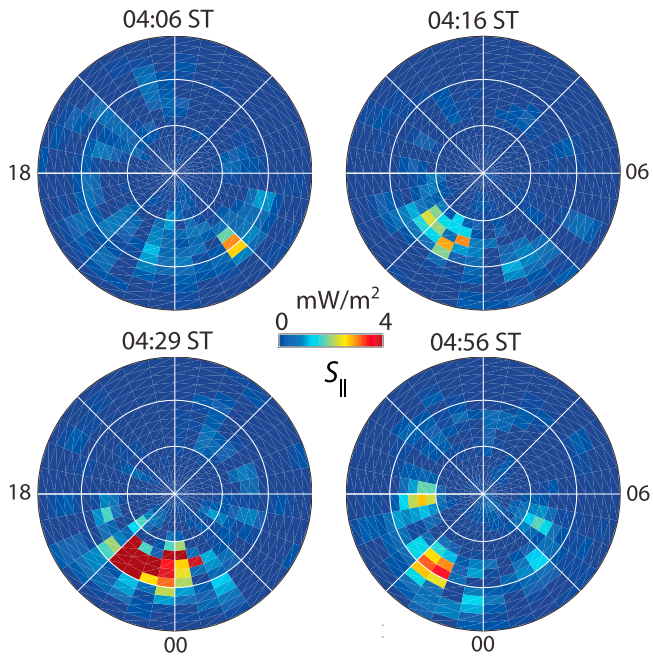

Figure 2. Four snapshots of instantaneous Alfvénic Poynting flux derived from the controlled LFM simulation and mapped to the reference altitude of 100 km.

mapped to 100-km altitude from the inner simulation boundary during the last hour of the idealized simulation. Thus the average patterns of downward Alfvénic Poynting flux exhibited in Figures 1b and 3a (discussed next) are actually ensembles of temporally and spatially varying Alfvén-wave packets or bursts.

[24] Figure 3a shows the distribution of 1-hour averaged, downward Poynting fluxes for the controlled simulation plotted in the same format as Figure 1b and calculated using the same procedure, except that the 1-hour average of $S_{\|}$ makes it unnecessary to compute 1-minute averages of $S_{\|}$ to remove standing waves. The most intense Alfvénic Poynting fluxes flow into the nightside auroral zone between 2100–2400 MLT and 74°–82° MLAT.

[25] In contrast with the simulation results in Figure 1b, little downward Poynting flux flows into the cusp region in the controlled simulation. The relative absence of dayside Alfvénic activity is a consequence of the steady upstream driving conditions in the controlled simulation, which minimally disturb the subsolar magnetopause and produce little Alfvén-wave activity there. Since the subsolar magnetopause is magnetically connected to the low-altitude cusp, Alfvén-wave activity is also weak in the low-altitude cusp. Alternatively, magnetopause buffeting by the time-variable upstream conditions in the 24-hour simulation generates considerable Alfvénic activity near the subsolar magnetopause and in the low-altitude cusp in Figure 1b.

[26] The simulated event (Figure 1b) and controlled simulation (Figure 3a) exhibit similar spatial distributions of average downward flowing Alfvénic Poynting flux in the premidnight auroral region. This result was initially surprising to us because the steady interplanetary conditions are symmetric in the idealized simulation. Statistical results from the Polar study (Figure 1a) also show a similar dawn-dusk asymmetry. The question therefore arises: What causes dawn-dusk asymmetry in the distribution of average downward Alfvénic Poynting flux on the nightside?

[27] The asymmetry in simulated Alfvénic power is due to meridional gradients in the ionospheric Hall conductance. In the LFM model, Pedersen and Hall conductances are calculated using the empirical relations derived by *Robinson et al.* [1987]. The energy flux and average energy of the precipitating electrons required to evaluate the Robinson et al. conductances are inferred from MHD variables near the low-altitude, spherical simulation boundary (see Appendix A and *Wiltberger et al.* [2009]). Enhancements in the ionospheric conductance are observed in regions of enhanced electron precipitation, especially in regions of upward field-aligned current density [*Robinson et al.*, 1985; *Ohtani et al.*, 2009]. These same enhancements occur in the LFM simulations, with diffuse precipitation producing enhanced conductance at lower latitudes and monoenergetic precipitation producing enhanced conductance most prominently where intense duskside region-1 currents flow out of the ionosphere [cf. *Wiltberger et al.*, 2009, Figure 6].

[28] To verify the effect of gradients in conductance on nightside Alfvénic power, a simulation with constant ionospheric conductance was performed using the same controlled solar wind and IMF conditions. Figure 3b shows the distribution of average downward Alfvénic Poynting flux derived from the test simulation in which the Pedersen and Hall conductances were taken to be constant throughout the simulation ionosphere with $\Sigma_P = 5$S,$\Sigma_H = 0$ S. When Σ_H is uniform in the simulation (either zero or non-zero), its constant value does not affect the coupling between the magnetosphere and ionosphere. The ionospheric Hall currents are divergence-free in this case and do not enter the solution of the electrostatic coupling equation (A1) given in Appendix A. As a result, in the controlled simulation with constant ionospheric conductance, Σ_H is simply set to zero. Numerical experiments with non-zero uniform Hall conductance show essentially the same results as those derived from the zero Hall conductance simulation. The simulation result shows that the dawn-dusk asymmetry in downward Alfvénic Poynting flux is eliminated by introducing constant conductance in the ionosphere. To determine how the gradient in ionospheric conductance regulates the distribution of Alfvénic power, we now examine the generation of Alfvénic power in the magnetotail.

4. Generation of $S_{\|}$ in the Magnetotail

[29] A synoptic map showing the near equatorial distribution of 1-hour averaged, earthward-flowing $S_{\|}$ in color, evaluated on the $z = 0.25$ R_E plane, is shown in Figure 3c for the controlled simulation corresponding to Figure 3a. MHD velocity vectors (v_x and v_y components in black) and the $B_z = 0$ contour (white line), both evaluated in the equatorial ($z = 0$) plane, are overlaid on the $S_{\|}$ distributions. The spherical inset shows the $S_{\|}$ distribution on a geocentric sphere at 3.6 R_E, produced by mapping $S_{\|}/B$ = constant from 100-km altitude in Figure 3a upward along dipole field lines to the 3.6 R_E sphere. In the synoptic plot, 6-sec averages of E and B derived from 1-sec samples are used in the calculation rather than 5-sec samples as was done in constructing Figure 1b, but as noted above, this choice makes

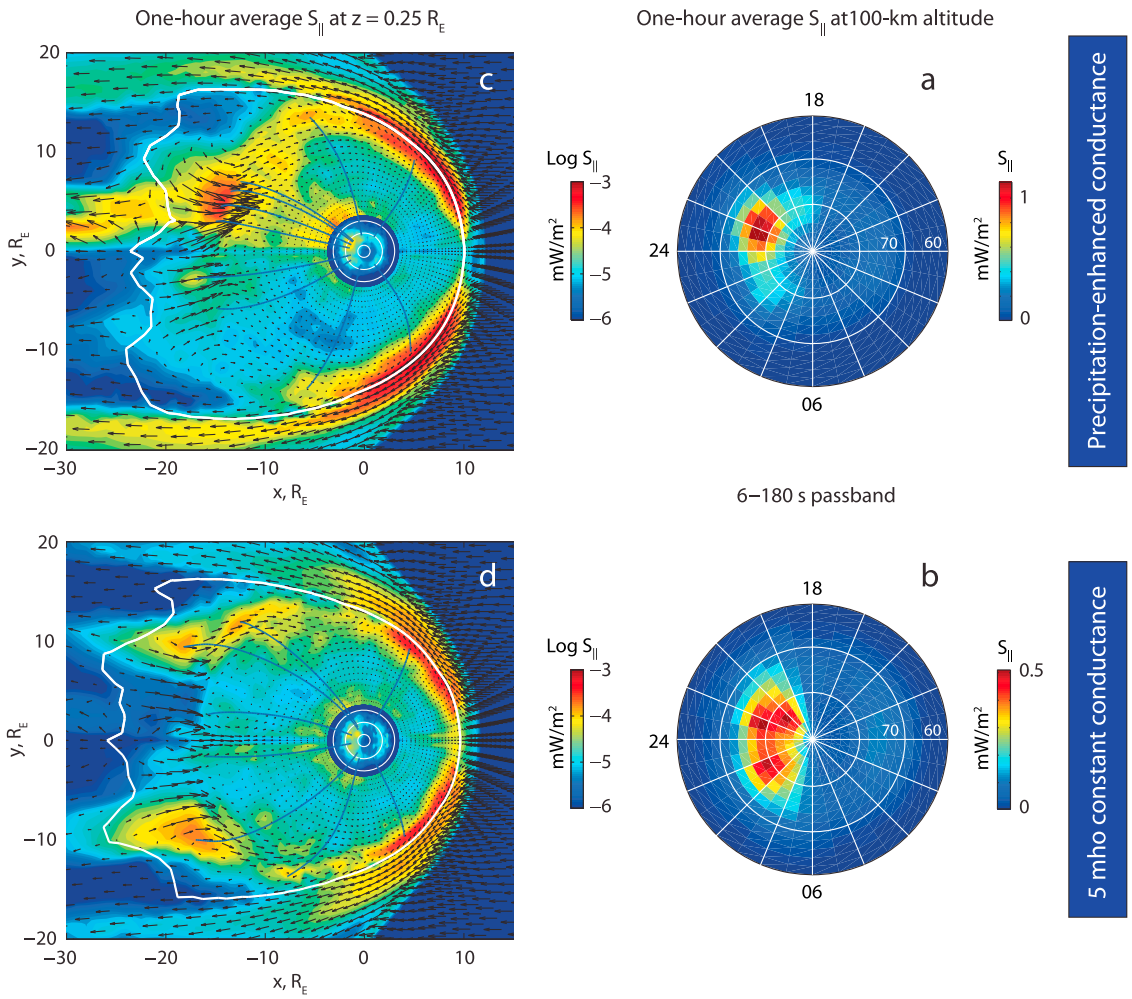

Figure 3. Distributions of 1-hour averaged downward Alfvénic Poynting flux mapped to the 100-km reference altitude from the controlled simulation with (a) electron precipitation-enhanced ionospheric conductances and (b) 5 mho constant ionospheric conductances. (c and d) Corresponding nightside equatorial plasma sheet fields with flow vectors (black), $B_z = 0$ contour (white) and magnetic field lines using average B-field (blue) overlaid on $\log_{10}S_{\|}$ in color. The spherical inset shows the distribution of $\log_{10}S_{\|}$ on a geocentric sphere at 3.6 R_E, produced by upward mapping of $S_{\|}/B$ = constant along dipole field lines from the ionosphere altitude of 100 km.

little difference in the end result; a 180-s running average of **E** and **B** is subtracted to give the perturbation fields, δ**E** and δ**B**, required to evaluate $S_{\|}$ in equation (1), for both the ionospherically mapped distribution of $S_{\|}$ and its plane distribution at $z = 0.25$ R_E. Finally, selected magnetic field lines, calculated from the 1-hour average B-fields at each simulation grid cell, are traced between the $z = 0.25$ R_E plane and the $r = 3.6$ R_E sphere to illustrate connectivity of $S_{\|}$ between the regions of interest. Note that the log-scale color bar of the spherical inset reveals small-amplitude features in the $S_{\|}$ distribution that are less evident when plotted using a linear-scale color bar as in Figure 1b or 3a.

[30] As mentioned above, the most intense Alfvénic Poynting fluxes in the controlled simulation are generated along the magnetopause flanks by Kelvin-Helmholtz surface waves and in the magnetotail (dominantly premidnight in this simulation) by time-variable, braking fast flows emerging from nightside reconnection [*Angelopoulos et al.*, 1992]. The Alfvénic Poynting fluxes reaching low altitude from the magnetotail sources are more intense than those from the flankside sources due to the lensing effect of converging magnetic flux tubes. The flux tube convergence and the effective lensing power is greater between the magnetotail and the ionosphere than between the magnetopause boundary region and the ionosphere. Let subscripts I, MT and MP, denote ionosphere, equatorial magnetotail and equatorial magnetopause regions, respectively. Along sample field lines in Figure 3c, we find $B_I/B_{MT} = 4320$ and $B_I/B_{MT} = 675$. Thus for Poynting fluxes of the same intensity in the magnetotail and near the magnetopause, conservation of field-aligned electromagnetic energy flow ($S_{\|}/B$ = constant) and the greater convergence of magnetotail flux tubes yields fluxes at the base of magnetotail flux tubes that are 6.4 × larger than those at the base of magnetopause boundary layer flux tubes. Some of the difference might also be due to diversion of a greater portion of the magnetopause-region field-aligned

Poynting flux into thermal or kinetic MHD energy flux or perpendicular Poynting flux as it flows toward the ionosphere (not investigated).

[31] For comparison, Figure 3d shows the equatorial-region synoptic plot corresponding to the simulation with a 5 S, constant Pedersen conductance ionosphere (Figure 3b). The dawn-dusk asymmetry evident in Figure 3c is absent in Figure 3d. The enhancements and/or gradients in ionospheric conductance produced by electron precipitation evidently modify the distributions and intensities of the field-aligned currents and the Poynting fluxes flowing between the ionosphere and the magnetotail. Compared with Figure 3d, the $S_{\|}$ in Figure 3c is more intense and extends over a larger range of MLT on the dayside, which might be a consequence of higher dayside conductance in Figure 3c.

[32] The time variability in plasma sheet convection is responsible for generating the time-variable Poynting fluxes shown in Figure 3. The dawn-dusk asymmetry in Poynting flux is controlled by the dawn-dusk asymmetry in simulated plasma sheet convection. Statistical averages of plasma sheet convection derived from satellite data exhibit a similar dawn-dusk asymmetry [*Nakamura et al.*, 1991; *Raj et al.*, 2002; *Guild et al.*, 2008; *Juusola et al.*, 2011; *McPherron et al.*, 2011]. The simulations show that the asymmetry is ultimately controlled by the MI interaction. The closure of field-aligned current flowing between the two regions regulates the flow channelization across the plasma sheet and determines the extent of earthward penetration and spatial variation of the fast flow. Thus plasma sheet dynamo and ionospheric load characteristics and the electromagnetic power flows between them are also controlled by the MI interaction [*Haerendel*, 2009].

[33] A more extensive analysis of the physical mechanisms of the MI coupling processes manifested in Figure 3 will be reported separately. It is sufficient to note here that the processes that control the distribution and intensity of the duskside fast flow channel also control the distribution and intensity of the Alfvén-wave power flowing into the ionosphere. The comparison between Figures 3c and 3d clearly reveals the importance of electron precipitation and its effects on ionospheric conductance in regulating the dawn-dusk asymmetry of plasma sheet convection and earthward-flowing MHD wave power.

5. Propagation From the Plasma Sheet

[34] To evaluate more definitively the mode of propagation, we show in Figure 4 simulation diagnostics for the controlled simulation. The positions of two stationary point probes are shown in Figure 4a, together with the instantaneous magnetic field lines connecting the probes and the ionosphere. Probe A is located in the premidnight plasma sheet region at $(X_{GSM}, Y_{GSM}, Z_{GSM}) = (-14.4, 4.5, 0.25)R_E$. Probe B is located in the inner magnetosphere at $(-5.4, 3.5, 5.2)$ R_E. The polar Poynting flux distribution at $r = 2.06$ R_E near the low-altitude boundary of the simulation (surface C) is also shown at time 04:28 ST.

[35] The time-bursty Poynting flux recorded at simulation probes A and B is shown in Figure 4b. The Alfvén wave packet carrying the Poynting flux takes about 145 s to propagate from probe A to probe B (that the packet at probe B propagates as a shear Alfvén wave is demonstrated below). As shown in Figure 4a, in this time the magnetic flux tube, along which the wave pulse propagates, convects earthward from the location of probe B to the location shown in Figure 4a at 04:27:05 ST. The effective velocity of the shear Alfvén wave packet therefore includes two components: one due to wave propagation along the ambient magnetic field and one due to convection across the magnetic field [*Mallinckrodt and Carlson*, 1978]. The smaller pulse amplitude (≈1/6) recorded in the Poynting flux at probe B relative to that at probe A is consistent with electromagnetic power being carried mainly in the fast MHD mode at probe A and mainly in the shear Alfvén mode at probe B, with only a small fraction of the power at probe A going into the shear Alfvén mode. The fast mode propagation is essentially isotropic, so the wave power decreases as r^{-2} with distance from a fast mode source. The fast mode power at probe B would be a small fraction of that at probe A if fast mode power is generated by time variable reconnection at the approximate location of the $B_z = 0$ contour in Figure 4a. Another possible reason for the smaller magnitude of $S_{\|}$ recorded at probe B is numerical dissipation. In the LFM simulation with the specific resolution used in this study, wave components with frequency greater than 50 mHz are damped numerically.

[36] In the LFM simulation, the phase speed of propagation of an Alfvén wave is limited by the *Boris* [1970] correction, which includes the effect of the perpendicular displacement current. The resulting linear dispersion relation gives the following values for $\delta E_{\perp}/\delta B_{\perp}$ for propagating shear Alfvén and fast modes:

$$\frac{\delta E_{\perp}}{\delta B_{\perp}} = \frac{\omega}{k_{\|}} = v_{\|} \begin{cases} 1 & \text{Alfvén wave} \\ 1/\cos\theta & \text{Fast mode} \end{cases} \tag{2}$$

with $v_P \approx v_A/\sqrt{1 + v_A^2/c^2}$. The above expression for the fast mode is valid when either $c_s^2/v_P^2 \ll 1$ or $v_A^2/c^2 \gg 1$; c_s and v_A are the sound and Alfvén speeds, respectively; c is the speed of light in vacuum. To satisfy numerical constraints in the simulation (principally the Courant condition on the time step), c is set to 1100 km/s in the Boris correction. At probe (A, B), the simulation results give $v_A/c \approx (2.5, 100)$. Thus $v_P \approx c$ at both probes in the LFM simulation, and the condition for (2) to be valid for the fast mode is satisfied. The parallel phase speed of a shear Alfvén wave propagating between probes A and B, and the ratio $aE_{\perp}/\delta B_{\perp}$ for a propagating Alfvén wave, are essentially constant in the simulation with value c.

[37] Figure 4c shows $|\delta E_{\perp}(f)|/|\delta B_{\perp}(f)|$ versus frequency, normalized to v_P, at probe A in the duskside plasma sheet ($|\cdot|$ indicates modulus of the complex amplitude). The frequency dependent, complex electric and magnetic perturbations are derived from Fourier transforms of the recorded amplitudes for $\delta E_{\perp}(t)$ and $\delta B_{\perp}(t)$ in a 5-minute interval surrounding the time 04:24:40 ST when the Poynting flux burst in Figure 4b was recorded at probe A. The ratio $|\delta E_{\perp}(f)|/|\delta B_{\perp}(f)|$ in Figure 4c is greater than the effective Alfvén speed (1) in the MHD simulation, suggesting that the Poynting flux burst recorded at probe A is carried by the MHD fast mode. The color band in Figure 4c shows the expected range of the phase speed for a propagating fast mode wave in the simulation when $60° < \theta < 80°$.

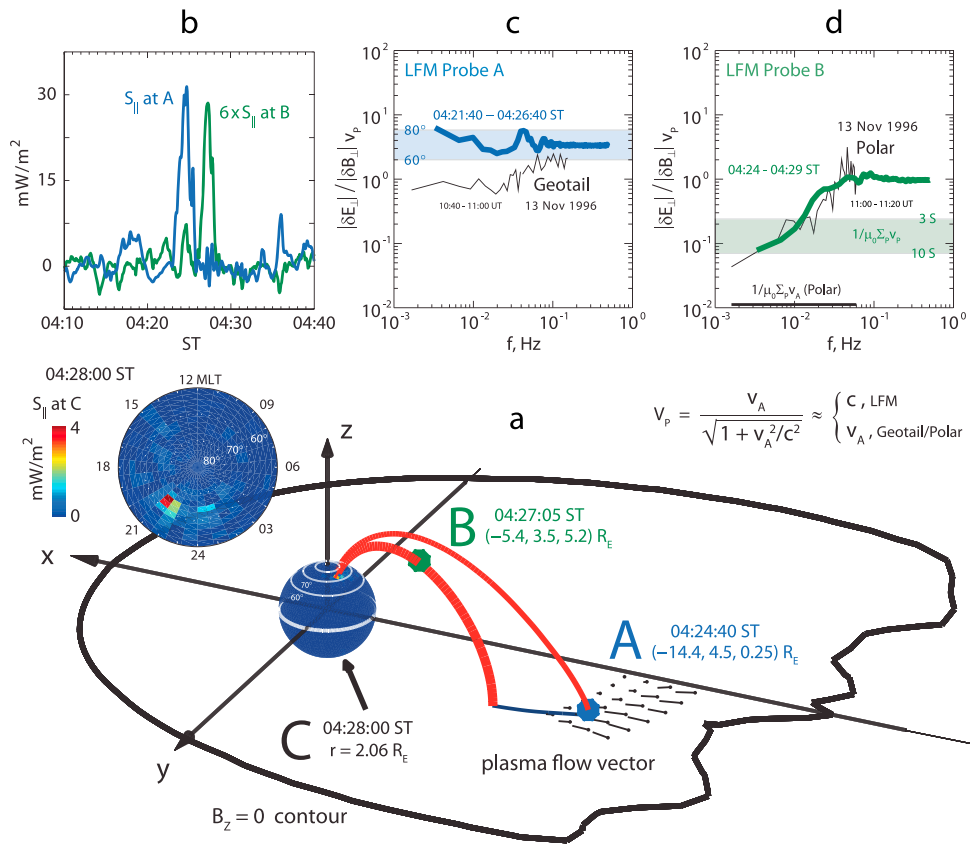

Figure 4. (a) The positions of two stationary probes A and B in the magnetosphere together with the instantaneous magnetic field lines connecting the probes and the ionosphere, average plasma flow vector in the equatorial plane and $B_z = 0$ contour. The polar plot shows the instantaneous distribution of $S_{\parallel}$ at the ionospheric altitude of 100 km at 04:28:00 ST (simulation time). The time indicated at probes A and B shows the simulation time of maximum $S_{\parallel}$ recorded at the corresponding probe position. The sphere C shows the distribution of $S_{\parallel}$ on a geocentric sphere at $r = 2.06$ R_E, produced by upward dipole mapping of $S_{\parallel}/B$ = constant from the ionosphere altitude. (b) The Alfvénic Poynting flux $S_{\parallel}$ recorded by probes A (blue) and B (green) as a function of time and mapped to the reference altitude of 100 km assuming $S_{\parallel}/B$ = constant. (c) The blue curve shows $|\delta E_{\perp}(f)|/|\delta B_{\perp}(f)|$ versus frequency, normalized to the phase velocity v_P, at probe A from the simulation. The black curve shows the same quantity observed on 13 Nov 1996 by the Geotail satellite at (−18,2,−3) R_E. The color band shows the expected range of the phase speed v_P of a propagating fast mode wave for $60° < \theta < 80°$. (d) The green curve shows $|\delta E_{\perp}(f)|/|\delta B_{\perp}(f)|$ versus frequency at probe B from the simulation. The black curve shows the same quantity observed on 13 Nov 1996 by the Polar satellite at (−4,5,−3) R_E. The color band shows the expected range for $|\delta E_{\perp}(f)|/|\delta B_{\perp}(f)| = 1/\mu_0\Sigma_P$ when 3 S $< \Sigma_P <$ 10 S.

[38] The simulated spectrum of $|\delta E_{\perp}(f)|/|\delta B_{\perp}(f)|$ shown in Figure 4d is derived from Fourier transforms of $\delta E_{\perp}(t)$ and $\delta B_{\perp}(t)$ in a 5-minute interval surrounding the time 04:27:05 ST when the Poynting flux burst in Figure 4b was recorded at probe B. The spectrum consists of two components. Above 50 mHz, it asymptotes to the constant value, $v_P \approx c$. This region of the spectrum is due primarily to the propagating Alfvén wave pulse evident in Figure 4b. The spectrum below 50 mHz increases with frequency. This type of variation in $|\delta E_{\perp}(f)|/|\delta B_{\perp}(f)|$ arises from a superposition of downward and upward propagating waves, with the upward propagating component produced by reflection from the ionosphere [*Knudsen et al.*, 1992; *Nagatsuma et al.*, 1996]. Reflection occurs at the low-altitude simulation boundary at $r = 2$ R_E where the ionospheric boundary condition is imposed. This standing wave component of the spectrum is evident in Figure 4b as the quasiperiodic waveform preceding the Alfvén wave pulse at probe B. The standing wave spectrum of $|\delta E_{\perp}(f)|/|\delta B_{\perp}(f)|$ should asymptote to $1/\Sigma_P$ as $f \rightarrow 0$ Hz, and the spectrum does shows some indication of bending toward an asymptote at the lowest resolved frequency of 3.3 mHz. If the asymptote is $1/\mu_0\Sigma_P$, the effective conductance at the ionospheric base of the flux tube must be greater than 10 S in the simulation. Time and spatial variations in the simulated electron precipitation cause Σ_P to vary between 3 S and 10 S during this pulse event. The boundary conditions on MHD variables at $r = 2$ R_E produces artificial reflection of waves incident on the boundary, which are not due just to ionospheric conductivity, so the effective conductance taking into account these artificial reflections may be higher than 10 S.

[39] MHD waves observed during a substorm on 13 Nov 1996 by the Polar satellite at (X_{GSM}, Y_{GSM}, Z_{GSM}) ≈ (−4, 5, 3)R_E and about 20 min earlier in the magnetotail by the Geotail satellite at (−18, 2,−3)R_E [*Angelopoulos et al.*, 2002] have been overlaid on the simulation curves ins Figures 4c and 4d. The solar wind and IMF conditions for this event are similar to those of the simulation but with variable and slightly weaker IMF B_z between −2 and −4 nT. $Kp = 2$ during the event. The Polar and Geotail satellites were in the same general regions, but not precisely at the same locations, of probes A and B in the simulation. The satellite data are superposed in the figures to illustrate the range of measured values for actual data. It is somewhat surprising that results from Polar and the LFM simulation in Figure 4d are so similar, especially given the use of the Boris correction in the simulation. The similarity may be fortuitous. A physical explanation implies that the Alfvén wave impedance, at both the Polar satellite and simulation Probe B, is dominated by standing waves at the lowest frequencies, and that the eigenmode structure is similar in both cases. Some portion of the low-frequency spectrum recorded at Geotail (Figure 4c) may include propagating Alfvén waves, particularly below 30 mHz where $\delta E_\perp/\delta B_\perp < v_A$. The observed ratio $\delta E_\perp/\delta B_\perp$ would be nearly equal to v_A at these lower frequencies if a 2.5% concentration of O^+ were present in the plasma sheet at the time of the Geotail observations. The simulation results suggest that at frequencies above 30–40 mHz Geotail may be seeing fast mode waves, although kinetic Alfvén waves may also be present as suggested by *Angelopoulos et al.* [2002].

[40] The simulation results are based on the equations of ideal one-fluid MHD and do not include the two-fluid, dispersive effects that produce kinetic Alfvén waves or kinetic effects that introduce Landau damping of kinetic Alfvén waves. Both effects may be operative in the Geotail and Polar fields reported by *Angelopoulos et al.* [2002]. Nevertheless, some basic features of the observed Alfvén wave event are captured in the simulation including: 1) generation of the Alfvén wave packet by a braking earthward flow burst; ii) similar variation in wave impedance versus frequency in the plasma sheet and at Polar satellite altitude; and iii) comparable ratio of magnetically mapped pulse amplitude in the plasma sheet to that at Polar altitude – factor of 6 in the simulation, factor of 10 in the event – even though the absolute intensity of the observed pulses is 6–40 × larger than that of the simulated pulses. The difference in absolute intensity is not surprising because smaller earthward flowing energy fluxes are expected during the simulated SMC conditions relative to the 13 Nov 1996 substorm conditions.

[41] The simulation results suggest a plausible alternative to the interpretation that the observed Poynting flux burst is carried mainly by kinetic Alfvén waves [*Angelopoulos et al.*, 2002]. In the simulation, the reduction in magnetically mapped amplitude between Geotail and Polar altitudes is not due to Landau damping of the Alfvén wave but to the fact that the signal is dominantly a fast compressional mode in the plasma sheet, although intermediate mode, shear Alfvén power is also present. The wave power at Geotail diminishes in its transit to Polar due to the more isotropic propagation of the fast mode, with its Poynting flux decreasing essentially as the inverse square of distance from the fast mode source. In contrast, the magnetic guidance of the Alfvén wave causes its Poytning flux to increase between Geotail and Polar in proportion to the ratio of the magnetic field intensity at the two measurement points along the field line. It is not surprising that a braking flow burst would generate substantial power in the compressional Alfvén mode. The fact that the wave impedance in the plasma sheet exceeds the Alfvén speed for the wave pulse reported by *Angelopoulos et al.* [2002], and that density and temperature perturbations appear during the interval of field-aligned Poynting flux bursts observed on Geotail [*Angelopoulos et al.*, 2002, Figures 7 and 10], are also consistent with the Poynting flux burst observed in the plasma sheet being carried mainly by fast mode waves. The apparent absence of elevated fluxes of field-aligned electrons at Polar and Geotail during the event is also consistent with the power at Geotail being dominantly fast mode.

[42] We conclude this section by noting that the simulated MHD wave dynamics are influenced by the artificial limit (1100 km/s) on the speed of light c imposed by the *Boris* correction. An alternative numerical experiment with the Boris speed of light set to c = 5500 km/s shows that the simulated magnetotail reconnection and flow velocity are different; however, the differences are small. Flow braking still occurs at approximately $X = -15$ R_E in the magnetotail when the LFM simulation is driven by the same upstream SW/IMF conditions as used in Figures 3 and 4. The magnitude and distribution of Alfvénic Poynting flux are similar to the results shown in Figure 2 and 3. Therefore, although MHD wave generation and propagation are influenced by the *Boris* correction, the dawn-dusk asymmetry, generation and propagation of Alfvénic Poynting flux are not dominated by the choice of c, and the conclusions derived from these simulations remain valid.

6. Conclusions

[43] The physics of the generation and propagation of bursty, nightside Alfvénic Poynting fluxes has been analyzed using global MHD simulation of the magnetosphere-ionosphere system. The power of both shear Alfvén and fast MHD waves is generated by braking bursty bulk flows stimulated by localized, time-variable magnetic reconnection in the magnetotail. Simulation results show that as the fast mode and shear Alfvén waves propagate earthward from their plasma sheet region of origin, the power in the compressional signal diminishes due to its essentially isotropic propagation, leaving a dominantly Alfvénic Poynting flux at lower altitudes on auroral field lines. Some observations suggest that this Alfvénic Poynting flux may be carried, at least in part, by kinetic Alfvén waves. Since two-fluid effects are not included in the simulation, the Alfvénic Poynting flux simulated here cannot be carried by kinetic Alfvén waves.

[44] When the LFM global simulation is driven by actual solar wind conditions, it reproduces with reasonable fidelity the observed statistical morphology and amplitude distribution of auroral and cusp-region Alfvénic Poynting fluxes reported by *Keiling et al.* [2003]. The cause of the observed enhancement in Alfvénic Poynting flux in the premidnight auroral sector relative to that in the postmidnight sector is due in part to asymmetries in the spatial distribution of ionospheric conductance. Enhancements in electron precipitation

and ionospheric conductance in the dusk sector induce higher fluxes of Alfvénic power in the premidnight sector. Controlled simulations show that when the ionospheric conductance is set to a constant, uniform value, the pre/postmidnight asymmetry in the distribution of earthward flowing Alfvénic power disappears.

[45] The controlled simulations also show that the ionospheric conductance, in response to precipitating particles from the magnetosphere, regulates the distribution of plasma sheet flow bursts during intervals of steady magnetospheric convection, with fast flows being more intense in the premidnight plasma sheet. To the extent that the global simulations adequately model the relevant underlying physics, we may therefore conclude that the distribution of ionospheric conductance has a great influence on magnetotail dynamics and structure, of which the generation of auroral Alfvénic power is just one manifestation.

[46] Despite the successes of the one-fluid simulations in capturing key features of auroral Alfvén dynamics, they do not include Alfvén wave dispersion and wave-particle interactions. We know that both effects can be important in the propagation and absorption of Alfvén wave power, particularly in boundary layers [*Hasegawa*, 1976] and at low altitudes where conversion of Alfvénic power to the precipitating electron power causes the Alfvénic aurora [*Chastonet et al.*, 2003]. Nonideal effects may also have other important consequences for energy conversion in the nightside reconnection exhaust flows that produce plasma sheet flow bursts.

Appendix A

A1. LFM Global Simulation

[47] The LFM global simulation uses a finite-volume method on a nonorthogonal grid to solve one-fluid, ideal MHD equations for evolution of mass, momentum and energy for the solar wind and magnetospheric plasmas. The solar wind-magnetosphere-ionosphere interaction is simulated with:

[48] 1. boundary conditions on the solar wind and interplanetary magnetic field at the sunward boundary of the computational domain;

[49] 2. a point dipole to represent Earth's magnetic field;

[50] 3. ionospheric electrodynamics, including a proxy for electron precipitation, at the inner (low-altitude) boundary.

[51] The simulation domain extends from X_{SM} = 30 R_E sunward to X_{SM} = −300 R_E anti-sunward, with a 100 R_E radial span in the $Y_{SM} - Z_{SM}$ plane. The variable cell size of the computational grid provides higher resolution near the bow shock, the magnetopause, in the magnetotail and near the low-altitude boundary, with lower resolution far from the earth in the solar wind and at the outer boundaries. The inner boundary is a sphere at a geocentric radial distance of 2 R_E where the electric drift velocity derived from electrostatic coupling to a 2-D ionosphere is imposed as a boundary condition on the fluid velocity [*Lyon et al.*, 2004].

A2. M-I Coupling Model

[52] The basic equation of the M-I coupling module combines Ohm's law with current continuity and the electrostatic approximation to obtain the following elliptic equation for the ionospheric electric potential Φ_i, given the field-aligned current density $J_{||i}$ at the top of the ionospheric conducting layer and the height-integrated conductance tensor $\underline{\Sigma}$:

$$\nabla \cdot \underline{\Sigma} \cdot \nabla \Phi_i = J_{||i} \cos\alpha. \tag{A1}$$

The equation is solved on a two-dimensional spherical surface located at 1.02 R_E geocentric [*Merkin and Lyon*, 2010]. The dip factor is $\cos\alpha = \hat{b} \cdot \hat{r}$ where $\hat{b}$ is a unit vector pointing along the dipole magnetic field at the top of the conducting layer and $\hat{r}$ is the radial unit vector in a spherical polar coordinate system with θ measured from the north pole. In addition to the limitations implied by the electrostatic approximation [*Lotko*, 2004], (A1) assumes the length scale for variation in θ satisfies $L_\theta \gg h|\tan\alpha|$ where $h \sim 100$ km is the effective height of the ionosphere.

[53] $J_{||i}$ is derived from the field-aligned current in the magnetosphere at the top surface (2.38 R_E) of the boundary cell, mapped to the top of the ionospheric conducting layer (1.02 R_E geocentric) along dipole field lines assuming $J_{||}/B$ = constant.

[54] The solution Φ_i is then mapped along dipole field lines to the low-altitude magnetospheric boundary, where the electric field, calculated as $\mathbf{E} = -\nabla\Phi_i$, serves as part of the low-altitude boundary condition for the MHD equations.

[55] The conductance tensor in (A1) may be represented in spherical polar coordinates as [*Merkin and Lyon*, 2010]

$$\underline{\Sigma} = \hat{\theta}\hat{\theta}\frac{\Sigma_P}{\cos^2\alpha} - \hat{\theta}\hat{\phi}\frac{\Sigma_H}{\cos\alpha} + \hat{\phi}\hat{\theta}\frac{\Sigma_H}{\cos\alpha} + \hat{\phi}\hat{\phi}\Sigma_P. \tag{A2}$$

Σ_P and Σ_H are the height-integrated Pedersen and Hall conductances. Empirical equations derived by *Robinson et al.* [1987] are used to modify the spatiotemporal distribution of the auroral contribution to ionospheric conductance, given the average energy flux F_ε and energy ε of electron precipitation derived from the LFM precipitation model. These empirical relations are

$$\Sigma_{P_{Auroral}} = \frac{40\varepsilon}{16+\varepsilon^2} F_\varepsilon^{0.5}, \tag{A3}$$

$$\Sigma_{H_{Auroral}} = 0.45\varepsilon^{0.85}\Sigma_P. \tag{A4}$$

[56] The conductance also includes a contribution from solar EUV ionization, which varies with solar zenith angle and the observed solar radio flux at 10.7 cm wavelength. The empirical models for $\Sigma_{P,H_{EUV}}$ are discussed in *Wiltberger et al.* [2004]. The total conductance is

$$\Sigma_{P,H} = \sqrt{\Sigma^2_{P,H_{Auroral}} + \Sigma^2_{P,H_{EUV}}}. \tag{A5}$$

A3. Electron Precipitation Model

[57] Precipitating electrons are assumed to be isotropic and Maxwellian in the magnetospheric source region, with allowance for acceleration along the magnetic field by a quasi-static potential drop V if the their thermal loss cone flux F_0 is insufficient to carry the MHD field-aligned current. Adiabatic kinetic theory gives the ionospheric number flux

of electrons precipitating in the loss cone [*Knight*, 1973; *Fridman and Lemaire*, 1980]:

$$F_N = F_0 \begin{cases} R_M - (R_M - 1)e^{-eV/T_e(R_M-1)}, & V > 0 \\ e^{eV/T_e}, & V < 0 \end{cases} \tag{A6}$$

$R_M = 8$ is the mirror ratio between the ionosphere and the electron source region (assumed to be located in the magnetosphere at the cell center of the low-altitude boundary of the MHD computation), T_e is the electron thermal energy in the source region, and V is the parallel potential drop. The thermal electron number flux in the loss cone without parallel acceleration $V = 0$) is

$$F_0 = N_e \left(\frac{T_e}{2\pi me} \right)^{1/2}. \tag{A7}$$

N_e is the electron density in the loss cone.

[58] The electron variables N_e and T_e are chosen to be proportional to the dynamically computed MHD density and temperature in each cell center at the low-altitude computational boundary:

$$T_e = aT_{\mathrm{MHD}}, \quad N_e = bN_{\mathrm{MHD}}. \tag{A8}$$

The empirical proportionality constants, $a = 1.72$ and $b = 0.023$, have been previously optimized for agreement between simulated and observed precipitation [*Fedder et al.*, 1995; *Slinker et al.*, 1999]. Parameter b effectively specifies the degree of loss cone filling in the source region.

[59] The field-aligned potential drop in (A6) has the form

$$V = \bar{\eta}\left|J_{||i}\right| \quad \text{with} \quad \bar{\eta} = \frac{T_e^{0.5}}{N_e}\mathcal{H}(J_{||i})\left[\mathrm{kV}/\left(\mu\mathrm{A/m}^2\right)\right]. \tag{A9}$$

The requirement that $V > 0$ for field-aligned currents flowing out of the ionosphere (upward) and $V < 0$ for downward currents is included in the step function

$$\mathcal{H}(J_{||}) = \begin{cases} \eta_\uparrow, & J_{||i} \text{ upward} \\ \eta_\downarrow, & J_{||i} \text{ downward} \end{cases} \tag{A10}$$

where $\eta_\uparrow = -5\eta_\downarrow = 11.25$ [*Fedder et al.*, 1995]. $\bar{\eta}$ has units of kV/(μA/m^2) when T_e is given in keV and N_e in cm^{-3}. Its density and temperature dependence are derived in the appendix of *Wiltberger et al.* [2009].

[60] Using (A6)–(A10), the average energy ε and energy flux F_ε needed to evaluate (A3) and (A4) are determined by

$$\varepsilon = T_e + eV \quad \text{and} \quad F_\varepsilon = \varepsilon F_N. \tag{A11}$$

[61] **Acknowledgments.** The research was supported by NASA under Heliophysics Theory Program Grant NNX11AO59G and Geospace Supporting Research and Technology Grant NNX11AJ10G, by the NSF National Space Weather Program Grant AGS-1023346, and by the Center for Integrated Space Weather Modeling funded by the NSF Science and Technology Centers program under cooperative agreement ATM-0120950. Computing resources for the research were provided by the National Center for Atmospheric Research under CISL projects 36761008 and 3761009. B. Zhang and W. Lotko would like to acknowledge the hospitality and support of the UCAR Advanced Study Program during summers 2009, 2011 when portions of the research were completed. The National Center for Atmospheric Research is sponsored by the National Science Foundation.

[62] Robert Lysak thanks the reviewers for their assistance in evaluating this paper.

References

Angelopoulos, V., W. Baumjohann, C. Kennel, F. Coroniti, M. Kivelson, R. Pellat, R. Walker, H. Lühr, and G. Paschmann (1992), Bursty bulk flows in the inner central plasma sheet, *J. Geophys. Res.*, *97*(A4), 4027–4039.

Angelopoulos, V., V. A. Sergeev, F. S. Mozer, K. Tsuruda, S. Kokubun, T. Yamamoto, R. Lepping, G. Reeves, and E. Friis-Christensen (1996), Spontaneous substorm onset during a prolonged period of steady, southward interplanetary magnetic field, *J. Geophys. Res.*, *101*(A11), 24,583–24,598.

Angelopoulos, V., J. A. Chapman, F. S. Mozer, J. D. Scudder, C. T. Russell, K. Tsuruda, T. Mukai, T. J. Hughes, and K. Yumoto (2002), Plasma sheet electromagnetic power generation and its dissipation along auroral field lines, *J. Geophys. Res.*, *107*(A8), 1181, doi:10.1029/2001JA900136.

Baumjohann, W., G. Paschmann, and H. Lühr (1990), Characteristics of high-speed ion flows in the plasma sheet, *J. Geophys. Res.*, *95*(A4), 3801–3809.

Boris, J. P. (1970), A physically motivated solution of the Alfvén problem, *Tech. Rep.*, *2167*, Nav. Res. Lab., Washington, D. C.

Chaston, C. C., J. W. Bonnell, C. W. Carlson, J. P. McFadden, R. E. Ergun, and R. J. Strangeway (2003), Properties of small-scale Alfvén waves and accelerated electrons from FAST, *J. Geophys. Res.*, *108*(A4), 8003, doi:10.1029/2002JA009420.

Claudepierre, S. G., S. R. Elkington, and M. Wiltberger (2008), Solar wind driving of magnetospheric ULF waves: Pulsations driven by velocity shear at the magnetopause, *J. Geophys. Res.*, *113*, A05218, doi:10.1029/2007JA012890.

Fairfield, D., et al. (1999), Earthward flow bursts in the inner magnetotail and their relation to auroral brightenings, AKR intensifications, geosynchronous particle injections and magnetic activity, *J. Geophys. Res.*, *104*(A1), 355–370.

Fedder, J. A., S. P. Slinker, J. G. Lyon, and R. D. Elphinstone (1995), Global numerical simulation of the growth phase and the expansion onset for substorm oserved by Viking, *J. Geophys. Res.*, *100*, 19,083–19,093.

Feldstein, Y. I., and G. V. Starkov (1967), Dynamics of auroral belt and polar geomagnetic disturbances, *Planet. Space Sci.*, *15*, 209–229, doi:10.1016/0032-0633(67)90190-0.

Fridman, M., and J. Lemaire (1980), Relationship between auroral electrons fluxes and field-aligned electric potential difference, *J. Geophys. Res.*, *85*(A2), 664–670.

Fuller-Rowell, T. J., and D. S. Evans (1987), Height-integrated Pedersen and Hall conductivity patterns inferred from the TIROS-NOAA satellite data, *J. Geophys. Res.*, *92*(A7), 7606–7618, doi:10.1029/JA092iA07p07606.

Guild, T. B., H. E. Spence, E. L. Kepko, V. Merkin, J. G. Lyon, M. Wiltberger, and C. C. Goodrich (2008), Geotail and LFM comparisons of plasma sheet climatology: 1. Average values, *J. Geophys. Res.*, *113*, A04216, doi:10.1029/2007JA012611.

Haerendel, G. (2009), Poleward arcs of the auroral oval during substorms and the inner edge of the plasma sheet, *J. Geophys. Res.*, *114*, A06214, doi:10.1029/2009JA014138.

Hardy, D. A., M. S. Gussenhoven, R. Raistrick, and W. J. McNeil (1987), Statistical and functional representations of the pattern of auroral energy flux, number flux, and conductivity, *J. Geophys. Res.*, *92*(A11), 12,275–12,294, doi:10.1029/JA092iA11p12275.

Hasegawa, A. (1976), Particle acceleration by MHD surface wave and formation of aurora, *J. Geophys. Res.*, *81*(28), 5083–5090, doi:10.1029/JA081i028p05083.

Juusola, L., N. Østgaard, and E. Tanskanen (2011), Statistics of plasma sheet convection, *J. Geophys. Res.*, *116*, A08201, doi:10.1029/2011JA016479.

Keiling, A., et al. (2000), Large Alfvén wave power in the plasma sheet boundary layer during the expansion phase of substorms, *Geophys. Res. Lett.*, *27*(19), 3169–3172, doi:10.1029/2000GL000127.

Keiling, A., J. R. Wygant, C. A. Cattell, F. S. Mozer, and C. T. Russell (2003), The global morphology of wave Poynting flux: Powering the aurora, *Science*, *299*, 383–386.

Kepko, L., M. Kivelson, and K. Yumoto (2001), Flow bursts, braking, and Pi2 pulsations, *J. Geophys. Res.*, *106*(A2), 1903–1915.

Knight, S. (1973), Parallel electric fields, *Planet. Space Sci.*, *21*, 741–750.

Knudsen, D., M. Kelley, and J. Vickrey (1992), Alfvén waves in the auroral ionosphere: A numerical model compared with measurements, *J. Geophys. Res.*, *97*(A1), 77–90.

Lotko, W. (2004), Inductive magnetosphere-ionosphere coupling, *J. Atmos. Sol. Terr. Phys.*, *66*(15–16), 1443–1456, doi:10.1016/j.jastp.2004.03.027.

Lyon, J. G., J. A. Fedder, and C. M. Mobarry (2004), The Lyon-Fedder-Mobarry (LFM) global MHD magnetospheric simulation code, *J. Atmos. Sol. Terr. Phys.*, *66*(15–16), 1333–1350, doi:10.1016/j.jastp.2004.03.020.

Lysak, R. L. (1990), Electrodynamic coupling of the magnetosphere and ionosphere, *Space Sci. Rev.*, *52*(1–2), 33–87, doi:10.1007/BF00704239.

Mallinckrodt, A., and C. Carlson (1978), Relations between transverse electric fields and field-aligned currents, *J. Geophys. Res.*, *83*(A4), 1426–1432.

McPherron, R. L., T.-S. Hsu, J. Kissinger, X. Chu, and V. Angelopoulos (2011), Characteristics of plasma flows at the inner edge of the plasma sheet, *J. Geophys. Res.*, *116*, A00I33, doi:10.1029/2010JA015923.

Merkin, V. G., and J. G. Lyon (2010), Effects of the low latitude ionospheric boundary condition on the global magnetosphere, *J. Geophys. Res.*, *115*, A10202, doi:10.1029/2010JA015461.

Nagai, T., M. Fujimoto, R. Nakamura, Y. Saito, T. Mukai, T. Yamamoto, A. Nishida, S. Kokubun, G. Reeves, and R. Lepping (1998), Geotail observations of a fast tailward flow at XGSM = -15 R_E, *J. Geophys. Res.*, *103*(A10), 23,543–23,550.

Nagatsuma, T., H. Fukunishi, H. Hayakawa, T. Mukai, and A. Matsuoka (1996), Field-aligned currents associated with Alfvén waves in the poleward boundary region of the nightside auroral oval, *J. Geophys. Res.*, *101*(A10), 21,715–21,729.

Nakamura, M., G. Paschmann, W. Baumjohann, and N. Sckopke (1991), Ion distributions and flows near the neutral sheet, *J. Geophys. Res.*, *96*(A4), 5631–5649, doi:10.1029/90JA02495.

Newell, P. T., T. Sotirelis, and S. Wing (2009), Diffuse, monoenergetic, and broadband aurora: The global precipitation budget, *J. Geophys. Res.*, *114*, A09207, doi:10.1029/2009JA014326.

Nishimura, Y., L. Lyons, S. Zou, V. Angelopoulos, and S. Mende (2010), Substorm triggering by new plasma intrusion: THEMIS all-sky imager observations, *J. Geophys. Res.*, *115*, A07222, doi:10.1029/2009JA015166.

Ohtani, S., S. Wing, G. Ueno, and T. Higuchi (2009), Dependence of premidnight field-aligned currents and particle precipitation on solar illumination, *J. Geophys. Res.*, *114*, A12205, doi:10.1029/2009JA014115.

Pulkkinen, T. I., M. Palmroth, H. E. J. Koskinen, T. V. Laitinen, C. C. Goodrich, V. G. Merkin, and J. G. Lyon (2010), Magnetospheric modes and solar wind energy coupling efficiency, *J. Geophys. Res.*, *115*, A03207, doi:10.1029/2009JA014737.

Raj, A., T. Phan, R. P. Lin, and V. Angelopoulos (2002), Wind survey of high-speed bulk flows and field-aligned beams in the near-Earth plasma sheet, *J. Geophys. Res.*, *107*(A12), 1419, doi:10.1029/2001JA007547.

Robinson, R. M., R. R. Vondrak, and T. A. Potemra (1985), Auroral zone conductivities within the field-aligned current sheets, *J. Geophys. Res.*, *90*(A10), 9688–9696.

Robinson, R. M., R. R. Vondrak, K. Miller, T. Babbs, and D. A. Hardy (1987), On calculating ionospheric conductivities from the flux and energy of precipitating electrons, *J. Geophys. Res.*, *92*, 2565–2569.

Sergeev, V., T. Bösinger, R. Belian, G. Reeves, and T. Cayton (1992), Drifting holes in the energetic electron flux at geosynchronous orbit following substorm onset, *J. Geophys. Res.*, *97*(A5), 6541–6548.

Sergeev, V. A., R. J. Pellinen, and T. I. Pulkkinen (1996), Steady magnetospheric convection: A review of recent results, *Space Sci. Rev.*, *75*(34), 551–604, doi:10.1007/BF00833344.

Shiokawa, K., W. Baumjohann, and G. Haerendel (1997), Braking of high-speed flows in the near-Earth tail, *Geophys. Res. Lett.*, *24*(10), 1179–1182.

Shiokawa, K., et al. (1998), High-speed ion flow, substorm current wedge, and multiple Pi 2 pulsations, *J. Geophys. Res.*, *103*(A3), 4491–4507, doi:10.1029/97JA01680.

Slinker, S. P., J. A. Fedder, B. A. Emery, K. B. Baker, D. Lummerzheim, J. G. Lyon, and F. J. Rich (1999), Comparison of global MHD simulations with AMIE simulations for the events of May 1920, 1996, *J. Geophys. Res.*, *104*(A12), 28,379–28,395, doi:10.1029/1999JA900403.

Volwerk, M., et al. (2007), Flow burst-induced Kelvin-Helmholtz waves in the terrestrial magnetotail, *Geophys. Res. Lett.*, *34*, L10102, doi:10.1029/2007GL029459.

Wiltberger, M., W. Wang, A. G. Burns, S. C. Solomon, J. G. Lyon, and C. C. Goodrich (2004), Initial results from the coupled magnetosphere-ionosphere-thermosphere model: Magnetospheric and ionospheric responses, *J. Atmos. Sol. Terr. Phys.*, *66*(15–16), 1364–6826, doi:10.1016/j.jastp.2004.03.026.

Wiltberger, M., R. S. Weigel, W. Lotko, and J. A. Fedder (2009), Modeling seasonal variations of auroral particle precipitation in a global-scale magnetosphere-ionosphere simulation, *J. Geophys. Res.*, *114*, A01204, doi:10.1029/2008JA013108.

Wygant, J., et al. (2000), Polar spacecraft based comparisons of intense electric fields and Poynting flux near and within the plasma sheet-tail lobe boundary to UVI images: An energy source for the aurora, *J. Geophys. Res.*, *105*(A8), 18,675–18,692.

Yasuhara, F., R. Greenwald, and S.-I. Akasofu (1983), On the rotation of the polar cap potential pattern and associated polar phenomena, *J. Geophys. Res.*, *88*(A7), 5773–5777, doi:10.1029/JA088iA07p05773.

Zesta, E., L. R. Lyons, and E. Donovan (2000), The auroral signature of earthward flow bursts observed in the magnetotail, *Geophys. Res. Lett.*, *27*(20), 3241–3244, doi:10.1029/2000GL000027.